Laser-assisted photoionization beyond the dipole approximation

R. Della Picca,[1,*] J. M. Randazzo,[1] S. D. López,[2] M. F. Ciappina,[3,4,5,†] and D. G. Arbó[2,6]

[1]*Centro Atómico Bariloche, CNEA, CONICET, and Instituto Balseiro, UNCuyo, 8400 Bariloche, Argentina*

[2]*Institute for Astronomy and Space Physics IAFE (UBA-CONICET), C1428ZAA Buenos Aires, Argentina*

[3]*Department of Physics, Guangdong Technion—Israel Institute of Technology, 241 Daxue Road, Shantou, Guangdong 515063, China*

[4]*Technion—Israel Institute of Technology, Haifa 32000, Israel*

[5]*Guangdong Provincial Key Laboratory of Materials and Technologies for Energy Conversion, Guangdong Technion—Israel Institute of Technology, 241 Daxue Road, Shantou, Guangdong 515063, China*

[6]*Facultad de Ciencias Exactas y Naturales and Ciclo Básico Común, Universidad de Buenos Aires, C1428EGA Buenos Aires, Argentina*

(Received 9 March 2023; accepted 20 April 2023; published 10 May 2023)

We present a theoretical study of atomic laser-assisted photoionization emission beyond the dipole approximation. By considering the nonrelativistic nondipole strong-field approximation (nondipole Gordon-Volkov wave function), we analyze the different contributions to the photoelectron spectrum, which can be written in terms of intra- and intercycle factors. We find that our nondipole approach not only exhibits asymmetric emission in the direction of light propagation, but also allows emission in dipole-forbidden directions. The former feature can be rooted in both intra- and intercycle interference processes, while the latter stems from a dependence of the sideband energy on the emission angle with respect to the propagation direction. Our theoretical scheme, presented here for He atoms in the 1*s* quantum state, is general enough to be applied to other atomic species and field configurations.

DOI: 10.1103/PhysRevA.107.053104

I. INTRODUCTION

When an extreme ultraviolet (XUV) pulse and an infrared (IR) laser field overlap in space and time with matter, the so-called laser-assisted photoionization emission (LAPE) processes take place. Here two main and distinct schemes can be distinguished depending on the XUV pulse duration, namely, (i) the streaking regime, when the XUV pulse is shorter than one IR optical cycle, and (ii) the sideband regime, when the XUV pulse is longer than one IR optical cycle. The XUV pulse promotes an electron wave packet to the continuum in the presence of the IR field. In (i), if both the XUV and IR fields are controlled with subfemtosecond time resolution, the photoelectron spectra for different time delays can be recorded. This *spectrogram* carries structural, amplitude, and phase information of both the XUV and IR fields. These parameters can be efficiently retrieved by applying well-established reconstruction algorithms [1–4]. Alternatively, in (ii), the concurrent absorption of one XUV photon, together with the exchange of one or more additional photons from the IR laser field, leads to equally spaced sideband (SB) peaks in the energy-resolved photoelectron spectrum (PES). They are located at higher and lower energies than the XUV photoionization energy value due to respective absorption and emission of IR photons [5,6]. The first theoretical prediction of the SB peaks was presented in [7]. Since then, a great deal of experimental and theoretical work has been reported in this field (see, e.g., [5,8–13] and references therein).

The sideband peaks have great similarities with the well-known above-threshold ionization (ATI) peaks in the context of multiphoton strong-field ionization, where the target absorbs more photons than those required for an electron to get ionized [14]. The formation of both kinds of peaks (ATI and SB) can be explained theoretically as the constructive interference between electron wave packets released at different optical cycles of the IR laser field [15–17].

Previously, we successfully identified electron trajectories and described the PES as a transparent product of inter- and intracycle interference factors based on the strong-field approximation (SFA) within the dipole approximation for both ATI [15,18,19] and LAPE scenarios [17,20,21]. We showed that the intercycle interference accounts for the sidebands' formation and the intracycle interference appears as a modulation of the former. These two types of interference can be easily explained as the coherent superposition of electron trajectories making use of the saddle-point approximation (SPA), for the calculation (time integration) of the transition matrix. However, resorting to the SPA is not necessary as we have shown in Refs. [22,23], where we have demonstrated that it is feasible to compute the PES as a function of a kernel quantity that represents the time-dependent photoionization transition matrix for an XUV pulse of only one IR cycle duration.

In all the above-described theoretical approaches, the dipole approximation was considered provided (i) the IR laser is weak enough and (ii) laser wavelengths (longer than atomic

*renata@cab.cnea.gov.ar

†marcelo.ciappina@gtiit.edu.cn

size) are short enough that consideration of magnetic effects can be neglected. Within the dipole approximation, photons transmit energy to the target (atom, molecule, or solid) but not momentum since the laser electric field is considered homogeneous with no contribution of the magnetic-field component. These assumptions must be revised when (i) ultrastrong laser fields [24] and (ii) mid-IR laser sources [25,26] are used. For long-wavelength high-intensity lasers, nondipole effects originate from the Lorentz force of the magnetic field and give rise to a momentum transfer of laser photons on the ejected electrons in the propagation direction. The contribution of relativistic effects in ATI can be quantified through the parameter [27–29]

$$q = \frac{U_p}{mc^2}, \tag{1}$$

which reflects the importance of the ponderomotive energy U_p, relative to the rest energy of the electron (m is the electron rest mass and c the speed of light). For small q and when the Coulombic effect of the remaining core on the photoelectron is disregarded, the classical motion of the ejected electron can be thought of as a composition of two motions: (i) The electron oscillates in the polarization direction due to the (dipole) laser electric field with the aforementioned ponderomotive energy and (ii) the electron drifts along the light propagation direction superimposed with an oscillation with twice the laser frequency with the well-known figure-eight motion, in a reference frame accompanying the electron in its average drift motion. The drift per cycle relative to the (dipole) quiver amplitude can be quantified as $\pi\sqrt{q}$ and the amplitude β_0 of the figure-eight motion along the propagation direction relative to the amplitude along the polarization direction as $\sqrt{q}/4$. A momentum shift along the laser propagation direction at the tunnel exit is a signature of the relativistic dynamics through the tunneling barrier in ATI [30]. Nondipole effects break the forward-backward symmetry of electron emission strongly reducing recollision in high-order above-threshold ionization affecting, therefore, photon emission by laser-driven ions [31].

The partitioning of the photon momentum transfer between the electron and ion is currently under debate [31–40]. Part of the photon momentum shift that the electron takes stems from the effect of the magnetic field during tunneling through the potential barrier formed by the atomic potential and the laser field. The remaining part of the photon momentum is transferred to the electron during its motion in the continuum [39–43]. For linear polarization, a shift of the low-energy region of the momentum distribution against the propagation direction has been reported [31,36,39]. Recently, it was shown that the subcycle linear momentum transfer can be explained through the interplay between nondipole and nonadiabatic effects on the tunneling dynamics [33]. Comparisons with experiments show that the laser beam profile must be considered together with nondipole effects to accurately describe the energy of the ATI peaks [43,44].

Despite the great and recent research activity of nondipole effects in strong-field ionization (see the works cited in the preceding paragraph), a detailed investigation of how the leading-order nondipole corrections affect the LAPE scenario is lacking. In this context, we consider (i) the absorption of one XUV photon followed by (ii) multiple absorption or emission of IR photons. Therefore, there is no possibility of momentum transfer of the IR photon to the atom at stage (i) and the IR photon momentum is only transferred during the photoelectron excursion in the continuum (ii). For this reason, in the current work, we study nondipole effects in LAPE. The aim of the present work is to unravel the nondipole traces in the PES structures that are encoded in both the intra- and intercycle interference patterns. We also analyze how nondipole effects shift the borders of the classically allowed region.

The paper is organized as follows. In Sec. II we briefly summarize the leading-order nondipole SFA theory and analyze the properties of the temporal integral of the transition matrix. In Sec. II A we analyze the intercycle contribution, then in Sec. II B we consider the intracycle factor, and finally in Sec. II C we analyze the semiclassical model for LAPE under nondipole conditions. In all cases, we scrutinize the asymmetry of the forward-backward emissions. A summary is presented in Sec. III. Atomic units are used throughout the paper, except where stated otherwise.

II. THEORY AND RESULTS

In the single-active-electron approximation, the time-dependent Schrödinger equation (TDSE) reads

$$i\frac{\partial}{\partial t}|\psi(t)\rangle = [H_0 + H_{\rm int}(t)]|\psi(t)\rangle, \tag{2}$$

where $H_0 = \mathbf{p}^2/2 + V(r)$ is the time-independent atomic Hamiltonian, whose first term corresponds to the electron kinetic energy and its second term to the electron-core Coulomb interaction. The second term on the right-hand side of Eq. (2), i.e.,

$$H_{\rm int} = [\mathbf{F}_X(\eta) + \mathbf{F}_L(\eta)] \cdot \left(\mathbf{r} - \frac{iz}{c}\boldsymbol{\nabla}\right), \tag{3}$$

describes the interaction of the atom with both time-dependent XUV $[\mathbf{F}_X(\eta)]$ and IR $[\mathbf{F}_L(\eta)]$ electric fields in the length gauge, with $\eta = \eta(t, \mathbf{r})$ [45]. We suppose the XUV pulse to be weak enough and of short wavelength well above the atomic size, i.e., $\omega_X \ll 2\pi c$, so that XUV ionization can be regarded within the dipole approximation, leaving the nondipole effects to the subsequent action of the IR laser, i.e., $\mathbf{F}_X(\eta) = \mathbf{F}_X(\omega_X t)$.

The electron initially bound in an atomic state $|\phi_i\rangle$ is emitted to a final continuum state $|\phi_f\rangle$, with final momentum $\mathbf{k}$ and energy $E = k^2/2$. Then the energy and angle-resolved photoelectron spectra can be calculated as

$$\frac{dP}{dE\,d\Omega} = \sqrt{2E}|T_{if}|^2, \tag{4}$$

where T_{if} is the T-matrix element corresponding to the transition $\phi_i \to \phi_f$ and $d\Omega = \sin\theta d\theta d\phi$ is the solid angle, with θ and ϕ the polar and azimuthal angles of the laser-ionized electron, respectively.

Within the time-dependent distorted-wave theory, the transition amplitude in the prior form is expressed as

$$T_{if} = -i\int_{-\infty}^{+\infty} dt\,\langle\chi_f^-(\mathbf{r}, t)|H_{\rm int}(\mathbf{r}, t)|\phi_i(\mathbf{r}, t)\rangle, \tag{5}$$

where $\phi_i(\mathbf{r},t)=\varphi_i(\mathbf{r})\,e^{iI_p t}$ is the initial atomic state, with ionization potential I_p, and $\chi_f^-(\mathbf{r},t)$ is the distorted final state. Equation (5) is exact as long as the final channel $\chi_f^-(\mathbf{r},t)$ is the exact solution of Eq. (2). However, several degrees of approximation have been considered so far to solve Eq. (5). The widest-known one is the SFA, which neglects the Coulomb distortion in the final channel produced on the ejected-electron state due to its interaction with the residual ion and disregards the influence of the laser field in the initial ground state [46,47]. The SFA, for instance, is able to model the ring structures of the ATI photoelectron spectrum [48].

In this work we consider the ionization of an atomic system by the combination of an XUV finite laser pulse assisted by an IR laser polarized in the (x,y) plane ($\hat{\varepsilon}_L$) and propagating in the $\hat{z}$ direction with wave vector $\mathbf{K}_L=K_L\hat{z}$. We describe the space- and time-dependent IR laser pulse by the vector potential as (see Sec. 2.8 of [45])

$$\mathbf{A}_L(\mathbf{r},t)=\mathbf{A}_L(\eta)=\hat{\varepsilon}_L A_L(\eta), \tag{6}$$

where $\eta=\omega_L t-\mathbf{K}_L\cdot\mathbf{r}=\omega_L(t-z/c)$ and the corresponding electric field is

$$\mathbf{F}_L(\eta)=-\frac{\partial}{\partial t}\mathbf{A}_L(\eta)=\hat{\varepsilon}_L F_L(\eta). \tag{7}$$

We are interested in the nondipole effects on the LAPE processes, which let us consider a space-dependent laser field at the lowest order in $1/c$ for the vector potential

$$\begin{aligned}\mathbf{A}_L(\eta)&\simeq\mathbf{A}_L(\eta)|_{\mathbf{r}=0}+(\mathbf{r}\cdot\nabla)\mathbf{A}_L(\eta)|_{\mathbf{r}=0}\\&\simeq\mathbf{A}_L(\omega_L t)+\frac{z}{c}\mathbf{F}_L(\omega_L t),\end{aligned} \tag{8}$$

where $\mathbf{A}_L(\eta)|_{\mathbf{r}=0}=\mathbf{A}_L(\omega_L t)$. Then we approximate the distorted final state with the nondipole Gordon-Volkov wave function in the length gauge [see Eq. (2.199) of [45]]

$$\begin{aligned}\chi_f^{V_{\rm ND}}(\mathbf{r},t)=(2\pi)^{-3/2}&\exp[i\mathbf{\Pi}(\mathbf{k},t)\cdot\mathbf{r}]\\&\times\exp\left[\frac{i}{2}\int_t^\infty\mathbf{\Pi}^2(\mathbf{k},t')dt'\right],\end{aligned} \tag{9}$$

where

$$\mathbf{\Pi}(\mathbf{k},t)=\mathbf{k}+\mathbf{A}_L(\omega_L t)+\left(\mathbf{k}\cdot\mathbf{A}_L(\omega_L t)+\frac{1}{2}\mathbf{A}_L^2(\omega_L t)\right)\frac{\hat{z}}{c} \tag{10}$$

and

$$\begin{aligned}\mathbf{\Pi}^2(\mathbf{k},t)=k^2&+2(\mathbf{k}\cdot\hat{\varepsilon}_L)\left(1+\frac{\mathbf{k}\cdot\hat{z}}{c}\right)A_L(\omega_L t)\\&+\left(1+\frac{\mathbf{k}\cdot\hat{z}}{c}+\frac{(\mathbf{k}\cdot\hat{\varepsilon}_L)^2}{c^2}\right)A_L^2(\omega_L t)\\&+\frac{\mathbf{k}\cdot\hat{\varepsilon}_L}{c^2}A_L^3(\omega_L t)+\frac{1}{4c^2}A_L^4(\omega_L t).\end{aligned} \tag{11}$$

Here we have taken into account that the IR contribution to the vector potential is dominant. As the frequency of the XUV pulse is much higher than the one of the IR field and considering the strength of the XUV field is much smaller than the IR one, the XUV contribution to the vector potential can be neglected [49,50]. Within the dipole approximation (in the $1/c\to 0$ limit), we can approximate the distorted final state with a Volkov function, which is the solution of the TDSE for a free electron in a homogeneous electromagnetic field [51].

With the appropriate choice of the IR and XUV laser parameters, we can assume that the energy domain of the LAPE processes is well separated from the domain of ionization by the IR laser alone. In other words, the contribution of IR ionization is negligible in the energy domain where the absorption of one XUV photon takes place and then $H_{\rm int}\simeq\mathbf{r}\cdot\mathbf{F}_X$. In addition, we set the general expression for the linearly polarized XUV pulse of duration τ_X as

$$\mathbf{F}_X(\omega_L t)=-\hat{\varepsilon}_X F_{X0}(t)\cos(\omega_X t), \tag{12}$$

where $\hat{\varepsilon}_X$ and ω_X are the polarization vector and the carrier frequency of the XUV field, respectively. Furthermore, $F_{X0}(t)$ is a nonzero envelope function during the temporal interval $(t_0,t_0+\tau_X)$ and zero otherwise, which we approximate as its maximum amplitude, i.e., $F_{X0}(t)\approx F_{X0}$. Thus, the matrix element of Eq. (5) can be written as

$$T_{if}=\int_{t_0}^{t_0+\tau_X}\ell(t)e^{iS(t)}dt, \tag{13}$$

where $S(t)$ is the generalized action

$$S(t)=(I_p-\omega_X)t+\frac{1}{2}\int^t\mathbf{\Pi}^2(\mathbf{k},t')dt' \tag{14}$$

and

$$\ell(t)=-\frac{i}{2}F_{X0}\hat{\varepsilon}_X\cdot\mathbf{d}[\mathbf{\Pi}(\mathbf{k},t)], \tag{15}$$

with the dipole moment defined as $\mathbf{d}(\mathbf{v})=(2\pi)^{-3/2}\langle e^{i\mathbf{v}\cdot\mathbf{r}}|\mathbf{r}|\varphi_i(\mathbf{r})\rangle$ (see the Appendix). In Eq. (13) we have used the rotating-wave approximation which in this case accounts for the absorption of only one XUV photon and thus neglects the contribution of XUV photoemission. In addition, during the XUV pulse time-lapse, the IR linearly polarized electric field can be modeled as a cosinelike wave and hence the vector potential can be written as

$$\mathbf{A}_L(\omega_L t)=\frac{F_{L0}}{\omega_L}\sin(\omega_L t)\hat{\varepsilon}_L, \tag{16}$$

where F_{L0} is the electric-field peak amplitude. Considering the T periodicity of the vector potential in Eq. (16), i.e., $T=2\pi/\omega_L$, and the $\mathbf{\Pi}$ dependence on time through $\mathbf{A}_L(\omega_L t)$, the dipole moment also fulfills

$$\mathbf{d}[\mathbf{\Pi}(t+jT)]=\mathbf{d}[\mathbf{\Pi}(t)] \tag{17}$$

for each integer number j.

Let us now analyze some features of the $T_{\rm if}$ matrix element (13). To this end we note that the action $S(t)$ defined in Eq. (14) can be written as

$$\begin{aligned}S(t)=&\,at+b\cos(\omega_L t)+f\sin(2\omega_L t)\\&+d\cos(3\omega_L t)+e\sin(4\omega_L t),\end{aligned} \tag{18}$$

where

$$
\begin{aligned}
a &= \frac{k^2}{2} + I_p - \omega_X + U_p\left(1 + \frac{\mathbf{k}\cdot\hat{z}}{c} + \frac{(\mathbf{k}\cdot\hat{\varepsilon}_L)^2}{c^2} + \frac{3U_p}{4c^2}\right),\\
b &= \frac{-F_{L0}}{\omega_L^2}(\mathbf{k}\cdot\hat{\varepsilon}_L)\left(1 + \frac{\mathbf{k}\cdot\hat{z}}{c} + \frac{3U_p}{2c^2}\right),\\
f &= \frac{-U_p}{2\omega_L}\left(1 + \frac{\mathbf{k}\cdot\hat{z}}{c} + \frac{(\mathbf{k}\cdot\hat{\varepsilon}_L)^2}{c^2} + \frac{U_p}{c^2}\right),\\
d &= (\mathbf{k}\cdot\hat{\varepsilon}_L)\frac{F_{L0}U_p}{6\omega^2c^2},\\
e &= \frac{U_p^4}{16\omega c^2}.
\end{aligned}
\tag{19}
$$

Here $U_p = (F_{L0}/2\omega_L)^2$ is the ponderomotive energy for homogeneous fields.

We then observe that $[S(t) - at]$ is a time-oscillating function with the same period T of the IR laser field, i.e.,

$$S(t + jT) = S(t) + ajT. \tag{20}$$

In light of these periodicity properties [Eqs. (17) and (20)], we can rewrite the transition matrix [Eq. (13)] in terms of the contribution of the first IR cycle only, as we have demonstrated in [22] within the dipole approximation. For that, let us introduce the kernel quantity $I(t)$ as the contribution to the transition amplitude from zero to time t, i.e.,

$$I(t) = \int_0^t \ell(t')e^{iS(t')}dt', \tag{21}$$

providing that $0 \leqslant t \leqslant T$. From its proper definition, it is clear that $I(t)$ increases from zero at $t = 0$ and depends on both the electron energy and the geometrical arrangement between $\hat{\varepsilon}_X$, $\hat{\varepsilon}_L$, $\hat{z}$, and the electron emission direction $\hat{k}$.

In a previous work [22] we presented the expression for the transition matrix as a function of the kernel quantity I for several cases of LAPE processes: streaking, sideband, and pulse train regimes. Since the development of those formulas is based on the same periodicity properties of Eqs. (17) and (20) in the present work, we finally find that in the nondipole situation Eqs. (18), (21)–(23), (33), and (36) of [22] remain valid. Among the three possible regimes, the sideband scenario is the most relevant since it is described as the product of two kinds of interferences, the intra- and intercycle contributions, while the other cases can be interpreted in light of these two factors but in a more complicated formula than a simple product. For that, in the present work we focus only on the SB regime (setting $\tau_X = NT$, with N an integer number and no XUV delay, i.e., $t_0 = 0$), where the PES is proportional to [see Eq. (23) of [22]]

$$\left|T_{if}^{\mathrm{SB}}\right|^2 = \underbrace{|I(T)|^2}_{\text{intracycle}} \underbrace{\left(\frac{\sin(aTN/2)}{\sin(aT/2)}\right)^2}_{\text{intercycle}}. \tag{22}$$

In the following, we analyze both the intra- and intercycle contributions beyond the dipole approximation. However, we keep our approach under the condition $q \ll 1$, i.e., a nonrelativistic description including nondipole effects. For this reason, in Eqs. (11) and (19) the terms of order $1/c^2$ will be neglected and only terms proportional to $\hat{z}/c$ are to be incorporated as a correction to the dipole approximation.

We consider the ionization of a He($1s$) as an example and we fix the IR polarization vector in $\hat{x}$ and the XUV one parallel to the IR propagation direction $\hat{z}$, i.e., $\hat{\varepsilon}_L = \hat{x}$ and $\hat{\varepsilon}_X = \hat{z}$. In Table I we show the rest of the laser parameters for several cases of study, chosen in such a way that $\omega_X - I_p - U_p = 2.596$ a.u., corresponding to the zeroth-order SB position, is identical for all cases.

Finally, we note that the scheme here presented can be easily extended to other, more sophisticated, models, e.g., the Coulomb-Volkov approximation, as long as $\mathbf{d}[\mathbf{\Pi}(t)]$ maintains the T periodicity and Eq. (17) is fulfilled.

A. Intercycle factor

The zeros of the denominator in the intercycle factor, i.e., the energy values satisfying $aT/2 = n\pi$, are avoidable singularities since the numerator also cancels out and maxima are reached at these points. Such maxima are recognized as the sidebands peaks in the PES. In the $1/c \to 0$ limit, i.e., within the dipole approximation, the sideband peak of order n occurs at $E_n^D = n\omega_L + \omega_X - I_p - U_p$, corresponding to the absorption ($n > 0$) or emission ($n < 0$) of n IR photons, following the absorption of one XUV photon. However, in the present case $aT/2 = n\pi$ leads to a quadratic equation for $k_n = \sqrt{2E_n}$: [see also Eq. (56) of Ref. [52]]

$$E_n = n\omega_L + \omega_X - I_p - U_p\left(1 + \frac{\mathbf{k}_n\cdot\hat{z}}{c}\right). \tag{23}$$

Rewriting this equation in terms of the parallel (k_{nz}) and perpendicular ($k_{n\perp}$) components of the electron momentum with respect to the propagation direction, we find

$$\frac{k_{n\perp}^2}{2} + \frac{1}{2}\left(k_{nz} + \frac{U_p}{c}\right)^2 \simeq n\omega_L + \omega_X - I_p - U_p \tag{24}$$

to $O(1/c)$, which can be understood as a ring in the momentum space with radius $\sqrt{2(n\omega_L + \omega_X - I_p - U_p)}$ and shifted an amount $-U_p/c$ in the $\hat{z}$ direction. Let us note that a similar result is obtained for the ATI peaks (see, for example, [36]). We observe that the new positions of the SB peaks are dependent on the projection of the emission direction into the IR propagation axis: $\mathbf{k}\cdot\hat{z} = k\cos\theta$.

In Fig. 1 we present the intercycle factor for case A (see Table I) as a function of the photoelectron energy and $\cos\theta$ at two energy ranges with ten sidebands each. In Fig. 1(a) we show that the sideband energies under the dipole approximation do not depend on the emission angle. Contrarily, the inclusion of nondipole effects produces the inclination of the sidebands [see Figs. 1(b) and 1(c)]. The vertical dashed lines indicate some reference values corresponding to SB peaks for certain orders n within the dipole approximation. When the emission is opposite to the IR propagation ($\cos\theta < 0$) the SBs are shifted towards higher energies. On the contrary, when $\cos\theta > 0$, the shift is in the direction of lower energies. This results in an emission asymmetry depending on whether the emission direction is parallel or antiparallel to the propagation direction of the laser. For each n order SB, the forward ($-$) and backward ($+$) energy shifts are

$$\Delta E \simeq \mp\frac{U_p}{c}\sqrt{2E_n^D}, \tag{25}$$

TABLE I. Laser parameters in atomic units for each case studied. Here $F_{X0} = 0.01$ and $\tau_X = NT$, with $N = 1$ or 2.

Case	F_{L0}	ω_L (λ_L)	U_p	ω_X	$\sqrt{q}$	$\beta_0 = q\ c/2\omega_L$
A	0.05	0.05 (911.26 nm)	1/4	3.75	$0.5/c$	$2.5/c$
B	$0.05/\sqrt{5} \simeq 0.02$	$0.05/\sqrt{5}$ (2037.6 nm)	1/4	3.75	$0.5/c$	$5.6/c$
C	$0.05/\sqrt{5} \simeq 0.02$	$0.05/\sqrt{10}$ (2881.6 nm)	1/2	4.0	$0.7/c$	$16/c$
D	$0.05/\sqrt{5} \simeq 0.02$	$0.05/\sqrt{20}$ (4075.3 nm)	1	4.5	$1/c$	$45/c$
E	$0.05/\sqrt{2} \simeq 0.03$	$0.05/\sqrt{12}$ (3156.7 nm)	3/2	5	$1.2/c$	$52/c$

respectively. We also observe that, according to Eq. (25), as the energy increases, the slope of the sidebands also increases: The sidebands of Fig. 1(c) are more slanted than in Fig. 1(b). Thus, the forward-backward asymmetry emission is more noticeable for higher energies. As sidebands are very robust structures throughout the focal volume [53], measuring the relative energy shift of sidebands, i.e., $\Delta E/\omega_L = \mp 2\beta_0\sqrt{2E_n^D}$, might be a helpful tool to determine the experimentally elusive intensity of strong and/or low-frequency IR lasers through the parameter $\beta_0 = qc/2\omega_L$.

B. Intracycle factor

In previous works, we have shown that the sideband structures stemming from the intercycle interferences are modulated by the intracycle factor [17]. Thus, in this section we analyze how the nondipole description affects the $|I(T)|^2$ modulation.

In Fig. 2(a) we show the intracycle factor multiplied by k for case A (see Table I) and for $\mathbf{k} = k_z\hat{z} + k_\perp\hat{x}$, i.e., emission in the (x, z) plane. This is equal to the PES (4), when $N = 1$. In Fig. 3 we show the PES for different cuts of the plots of Fig. 2: in Fig. 3(a) with θ fixed and in Fig. 3(b) at fixed energies as a function of the emission angle. We observe that the intracycle factor has a region delimited by certain energy and angle values and it vanishes outside this region. In a previous work [17] and within the semiclassical model, this fact was interpreted as a classically allowed region. As in the dipole description, inside the allowed region the intracycle factor has fringes. Comparing both the dipole and nondipole results, we do not observe significant qualitative differences in these fringes (not shown). However, due to the incorporation of nondipole terms of order $1/c$, we can expect that the most noticeable variations will be in the areas close to zero emission [white areas in Fig. 2(a)]. For that reason, we introduce in Fig. 2(b) the parameter A, which quantifies the

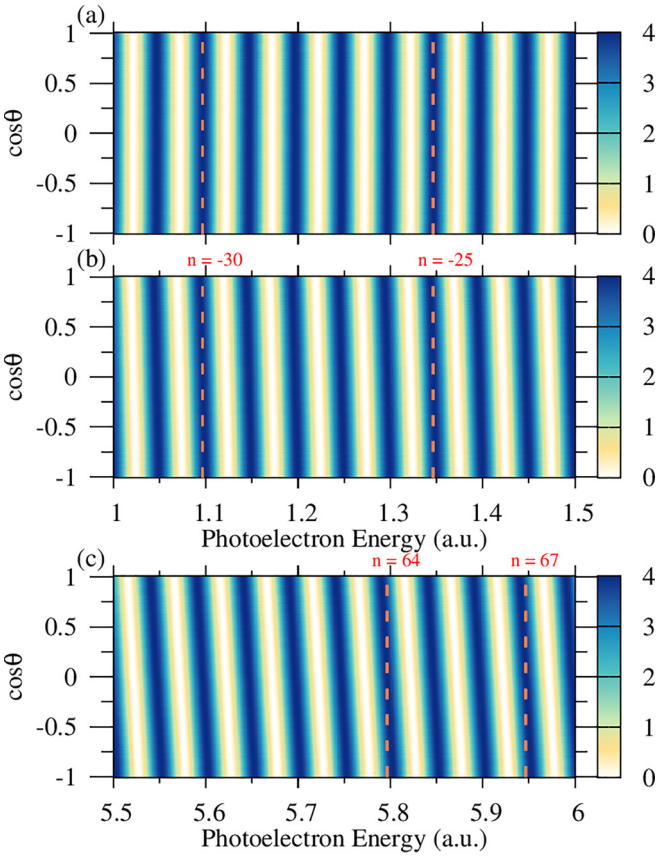

FIG. 1. Intercycle factor for case A (see Table I) parameters and $N = 2$, within the (a) dipole and (b) and (c) nondipole approximations. The vertical dashed lines indicate the position of the SB in the dipole approximation: E_n^D for (a) and (b) $n = -30, -25$ and (c) $n = 64, 67$.

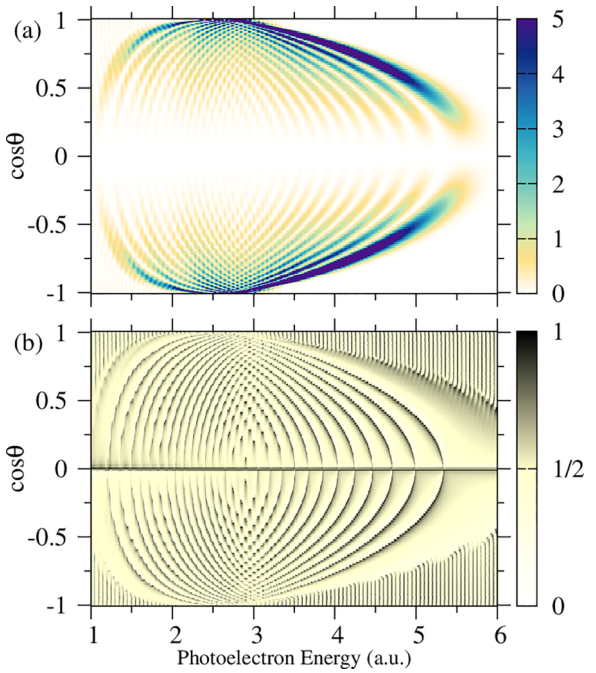

FIG. 2. (a) Nondipole LAPE PES (with $N = 1$) of He($1s$) for case A (see Table I) in logarithmic scale and arbitrary units. (b) Asymmetry factor (26).

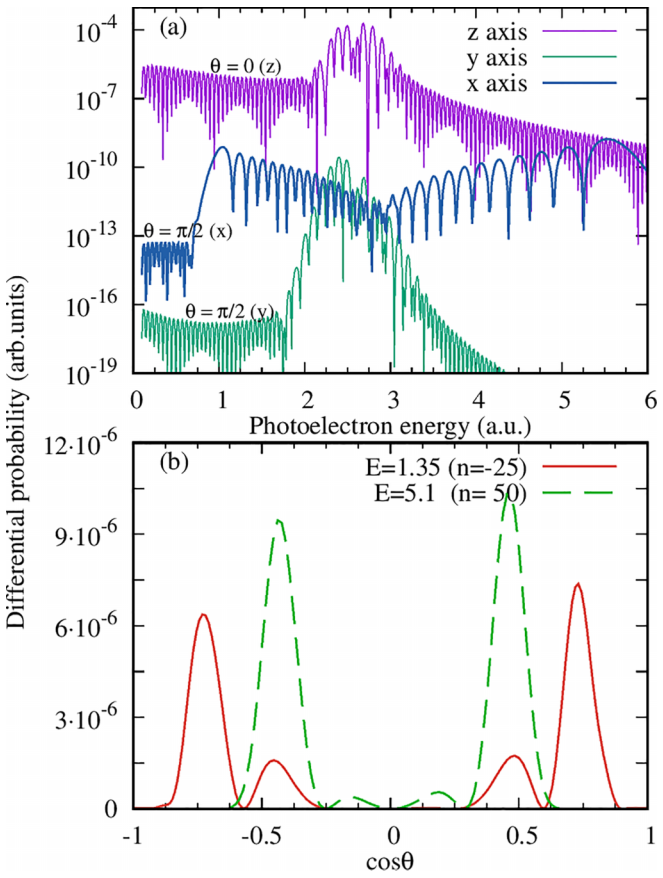

FIG. 3. Intracycle factor for LAPE of He(1s) for the nondipole case A (see Table I) at (a) fixed emission angles and (b) fixed energy values.

relative importance of nondipole effects

$$A(E,\theta) = \frac{\frac{dP^{\mathrm{ND}}}{dE d\cos\theta}}{\frac{dP^{\mathrm{ND}}}{dE d\cos\theta} + \frac{dP^{\mathrm{D}}}{dE d\cos\theta}}, \tag{26}$$

where ND and D correspond to the nondipole and dipole distributions, respectively. The parameter $A(E,\theta)$ will be 0 when nondipole effects are negligible, close to 1 when they are dominant, and $\frac{1}{2}$ when dipole and nondipole contributions are equal.

Close to the zero-emission areas [white region in Fig. 2(a)], we observe black or white areas in Fig. 2(b), featuring the nondipole contributions. We also recognize that the white structures in the lower half plane ($\cos\theta < 0$) become black in the upper one ($\cos\theta > 0$) and vice versa, which demonstrates the existence of an asymmetry in the forward-backward emission with respect to the IR propagation direction. This asymmetry can also be observed, for example, in Fig. 3(b), where the peaks on the right are higher than their respective ones on the left.

Therefore, we can conclude that (i) the forward-backward asymmetry emission is not circumscribed to the inclination of the sidebands (a proper contribution of the intracycle factor is also present) and (ii) the PES presents well-defined regions, where the emission probability is considerably higher, similar to the classically allowed regions for dipole LAPE. On the

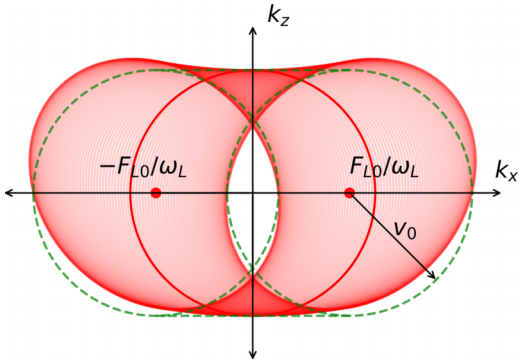

FIG. 4. Schematic classical limits in the momentum space (k_x, k_z). Green dashed lines depict the dipole results (see Ref. [17]).

borders of these regions, where the PES is close to zero, the $O(1/c)$ contribution will be noticeable. In this sense, it could be motivating to investigate if there are corrections in the classical limits due to nondipole effects. This is addressed in the next section.

C. Nondipole classical limits

The semiclassical model (SCM) consists in solving the time integral of Eq. (13) by means of the SPA, where the main contribution occurs for those times t_s for which the action is stationary, i.e., $dS/dt = 0$. In the nondipole approach, it means that [see Eq. (14)]

$$\mathbf{\Pi}^2(\mathbf{k}, t_s) = v_0^2, \tag{27}$$

where $v_0^2/2 = \omega_X - I_p$ corresponds to the mean energy of the photoelectrons ionized by the XUV pulse in the absence of the IR laser. Then the transition probability can be written as a coherent superposition of the amplitudes of all classical electron trajectories starting from stationary points t_s of the generalized action $S(t)$ with final momentum $\mathbf{k}$. Complex ionization times give rise to nonclassical trajectories with exponentially decaying factors and thus with minor relevance compared to classical trajectories with real values. In other words, those values of the momentum $\mathbf{k}$ satisfying Eq. (27) for real values of t_s define a region of classically allowed momenta. Considering the (k_x, k_z) plane and neglecting terms of the order of $1/c$ within the dipole approximation, we get an oscillating circumference, as it has been described in [17]. The oscillation is harmonic in the direction of the IR field, i.e., k_x, with amplitude F_{L0}/ω_L and frequency ω_L. In Fig. 4 we show these regions. At $t_s = 0$ we get the red circle, while the extreme regions correspond to the two green dashed circumferences. In the present case, the $O(1/c)$ contribution introduces a small correction. In order to make it visible, we have taken an artificial value of $c = 13.7$ to generate the red ellipses in Fig. 4. They come from the continuous movement and deformation of the circle as a function of t_s generated by the nondipole contributions.

As it was shown in [17] and comparing the quantum SFA and TDSE results, the SCM gives an excellent prediction where the PES is non-negligible. We can expect then a small nondipole variation in the classical limits. In order to analyze it, we consider the three principal directions $\hat{x}$, $\hat{y}$, and $\hat{z}$. In

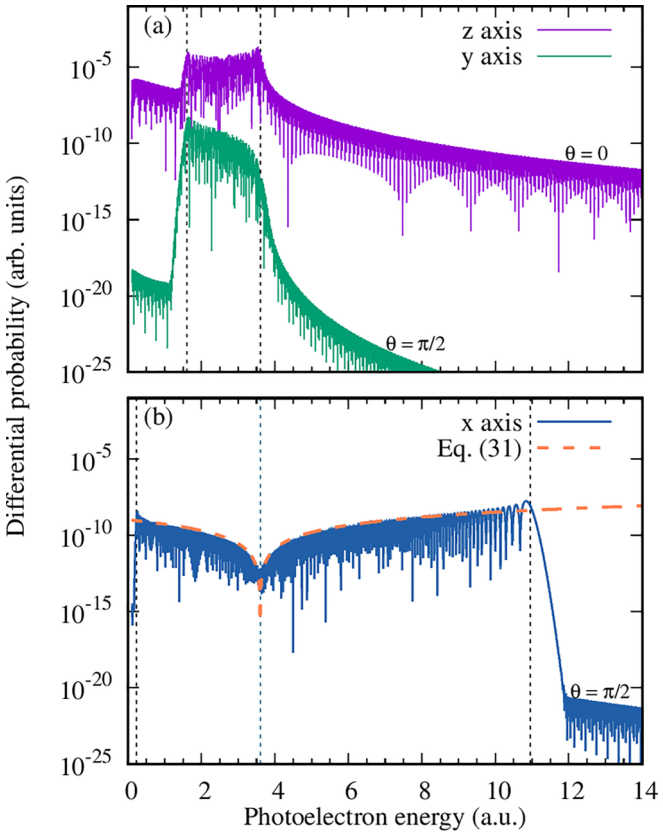

FIG. 5. Intracycle factor for case D as a function of the photoelectron energy at fixed emission angles. (a) The photoelectron momenta are $\mathbf{k} = k\hat{z}$ ($\theta = 0$) and $\mathbf{k} = k\hat{y}$ ($\theta = \pi/2$). The black dashed vertical lines indicate the semiclassical limit at $E_{\rm low} = 1.6$ a.u. and $E_{\rm up} = 3.6$ a.u. (b) The blue solid line shows $\mathbf{k} = k\hat{x}$ and the orange dashed line shows the quadratic approximation (31). The black dashed vertical lines indicate the semiclassical limit at $E_{\rm low} = 0.2$ a.u. and $E_{\rm up} = 11$ a.u. At $v_0^2/2 = 3.6$ a.u. (blue dashed vertical line) the PES shows a minimum.

Fig. 5 we show the intracycle factor for case D (see Table I) for emission in the $\hat{z}$ and $\hat{y}$ directions in Fig. 5(a) and $\hat{x}$ in Fig. 5(b). The vertical dashed lines indicate the classical limits obtained as follows. Equation (27) [neglecting $1/c^2$ terms in Eq. (11)] gives

$$v_0^2 = \begin{cases} k^2 + A_L^2 + \frac{A_L^2 k}{c} & \text{if (i) } \mathbf{k} = k\hat{z} \\ k^2 + A_L^2 & \text{if (ii) } \mathbf{k} = k\hat{y} \\ (k + A_L)^2 & \text{if (iii) } \mathbf{k} = k\hat{x}. \end{cases} \tag{28}$$

The maximum and minimum classically allowed k values are those for which the above equations have extreme values (maxima and minima) of the field $A_L(\omega_L t)$ or $A_L^2(\omega_L t)$. So, in case (ii), the values 0 and $(F_{L0}/\omega_L)^2 = 4U_p$ minimize and maximize the field $A_L^2(\omega_L t)$, respectively, giving rise to the classical limits $E_{\rm low} \simeq (v_0^2 - 4U_p)/2$ and $E_{\rm up} = v_0^2/2$. For case (iii), the limits are $E_{\rm low,up} = (v_0 \mp F_{L0}/\omega_L)^2/2$. These two cases (ii) and (iii) coincide exactly with those expected for the dipole approximation (see [17] for emission perpendicular and parallel to the dressing IR field). Instead, for case (i) there is a small nondipole correction to the dipole classical limit at low energy, whereas for $E_{\rm up} = v_0^2/2$ the lower limit is

$$E_{\rm low} = \frac{v_0^2}{2} - 2U_p\left(1 \pm \frac{1}{c}\sqrt{v_0^2 - 4U_p}\right). \tag{29}$$

We observe in Fig. 5 that, effectively, the larger emission probability is restricted to the SCM range, delimited by the classical borders $E_{\rm low,up}$.

The most striking difference compared with the dipole results lies in the fact that the emission in $\hat{x}$ is not forbidden [see Fig. 5(b)]. Indeed, in the dipole approximation, the dipole element $\mathbf{d}(\mathbf{k} + \mathbf{A})$ is orthogonal to the XUV polarization vector in $\hat{z}$ and then emission in the $\hat{x}$ direction is forbidden [23]. Instead, according to Eq. (A3), beyond the dipole approximation, we can expect some contribution of $O(1/c)$. Hence, all the contribution in this direction is purely nondipole. Furthermore, we can observe a very noticeable structure: a minimum at $E = v_0^2/2$. This structure can be easily understood in light of the semiclassical model: Since the principal contribution to the temporal integral occurs at real times t_s verifying Eq. (27), we can approximate $\ell(t)$ by

$$\begin{aligned} \ell(t_s) &\propto \frac{1}{c\left(v_0^2 + \alpha^2\right)^3}\left(kA_L(\omega_L t_s) + \frac{A_L^2(\omega_L t_s)}{2}\right) \\ &\propto \frac{v_0^2}{2} - \frac{k^2}{2}, \end{aligned} \tag{30}$$

where we have combined Eqs. (27), (28), and (A3). We note that this expression does not depend on the time t_s but on the energy $E = k^2/2$ and vanishes at the particular value $E = v_0^2/2$. Since it represents a zero of the matrix element, we can call it a Cooper-like minimum. Then the intracycle factor is proportional to a quadratic function of the energy that vanishes at the Cooper-like minimum:

$$|I(T)|^2 \propto |\ell(t_s)|^2 \sim \left(\frac{v_0^2}{2} - E\right)^2. \tag{31}$$

This quadratic function is plotted as a orange dashed line in Fig. 5(b), with an arbitrary normalization constant. The agreement is striking.

Now we want to explore the behavior of the intracycle factor and its relationship with the classical limits as a function of the laser configuration by increasing the q parameter, which indicates a growth of nondipole contributions. For that purpose, we consider cases B–E of Table I. In Fig. 6 we present the spectra for the three principal emission directions as previously considered. We observe that the spectra remain limited by the classical values and they widen as q increases. We also see that the qualitative shape of the spectra does not change and, notoriously, the Cooper-like minimum also persists [see Fig. 6(c)] at different energy positions as the XUV frequency varies.

Finally, we want to study if there is some kind of forward-backward asymmetry in the classical limits. For that we compare the emission in the parallel ($\hat{z}$) and antiparallel ($-\hat{z}$) directions with respect to the IR propagation direction. In Fig. 7 we compare both situations for case E. Very good qualitative agreement is observed at the entire range, except close

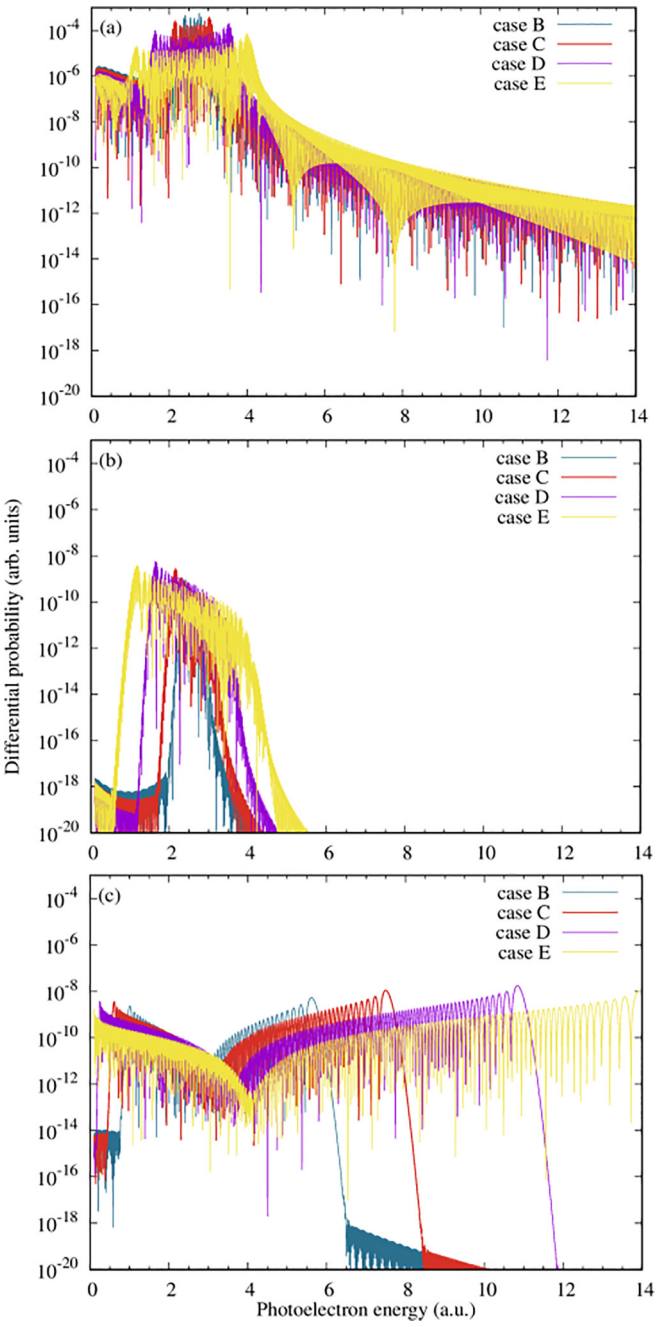

FIG. 6. Intracycle factor at the emission direction (a) $\mathbf{k} = k\hat{z}$, (b) $\mathbf{k} = k\hat{y}$, and (c) $\mathbf{k} = k\hat{x}$, for different laser parameters according to cases B–E (see Table I).

to the lower classical limit. According to Eq. (28),[1] the lower classical limits depend on the emission direction (forward or backward, i.e., $\pm\hat{z}$) according to Eq. (29). This small difference can be observed by comparing the forward and backward spectra: The solid curve rises before (at $E_{\text{low+}} = 1.06$ a.u.) the dashed one (at $E_{\text{low-}} = 1.13$ a.u.). Within the dipole

[1]The third term of this equation is negative for antiparallel emission.

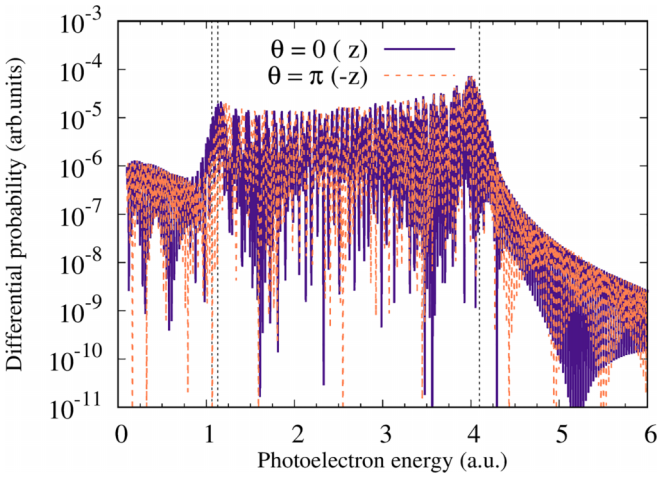

FIG. 7. Intracycle factor at the emission directions $\hat{z}$ (purple solid line) and $-\hat{z}$ (orange dashed line) for case E (see Table I). The dashed vertical lines indicate the classical limits at $E_{\text{low+}} = 1.06$ a.u., $E_{\text{low-}} = 1.13$ a.u., and $E_{\text{up}} = 4.09$ a.u.

approximation, both curves coincide exactly at the lower classical limit $E_{\text{low}} = 1.09$ a.u., which lies precisely in the middle of both (not shown).

Summarizing this section, we can say that the classical limits accurately determine the energy and emission angle range. These limits are slightly affected by nondipole effects. They appear as a forward-backward asymmetric emission. Moreover, beyond the dipole approximation, there is no restriction on the emission in the $\hat{x}$ direction; in this case, the semiclassical model predicts perfectly the shape of the spectra and the presence of a Cooper-like minimum at energy equal to $v_0^2/2$.

III. CONCLUSION

We have studied the laser-assisted photoemission process in a nonrelativistic SFA description including nondipole corrections. Due to the periodicity properties, in the same spirit of our previous work [22], we can rewrite the PES as a function of two principal contributions: the intra- and the intercycle factors. We have analyzed each factor and the modifications introduced in each of them by the nondipole effects. In order to consider a concrete case, we have analyzed the LAPE of He($1s$) in a particular geometrical arrangement of the XUV and IR polarization vectors and IR propagation direction, for several IR laser parameters. As a result of the intercycle interference, the sideband pattern exhibits an angle dependence (inclination), which increases with energy. The classical allowed angle-energy region, previously investigated within the dipole approximation, is sensitive to corrections of $O(c^{-1})$. As a particular point, we have found that the emission restriction in the $\hat{x}$ direction no longer holds in the nondipole approach. The nondipole semiclassical model shows excellent agreement with the SFA results and gives a useful interpretation of its most notorious structure, a Copper-like minimum. In both intra- and intercycle factors and also in the limits of the classically allowed region, we have observed and characterized a forward-backward asymmetry originated in the existence of

a privileged direction that is the IR propagation one. A more detailed analysis of this asymmetry deserves to be treated in future works.

ACKNOWLEDGMENTS

This work was supported by Grants No. PICT-2020-01755, No. PICT-2020-01434, and No. PICT-2017-2945 from ANPCyT (Argentina) and Grant No. PIP 11220210100468CO from CONICET (Argentina). M.F.C. acknowledges financial support from the Guangdong Province Science and Technology Major Project (Future functional materials under extreme conditions, Project No. 2021B0301030005) and the Guangdong Natural Science Foundation (General Program Project No. 2023A1515010871).

APPENDIX: TRANSITION-MATRIX DIPOLE ELEMENT

The dipole transition element is defined as

$$\mathbf{d}(\mathbf{v}) = \frac{1}{(2\pi)^{3/2}} \int d\mathbf{r} \exp(-i\mathbf{v}\cdot\mathbf{r})\mathbf{r}\phi_i(\mathbf{r}), \tag{A1}$$

where ϕ_i is a hydrogenlike bound state. For the case of a hydrogenic $1s$ state, we can write

$$\mathbf{d}(\mathbf{v}) = -\frac{i}{\pi} 2^{7/2}\alpha^{5/2} \frac{\mathbf{v}}{(v^2+\alpha^2)^3}, \tag{A2}$$

where $\alpha = \sqrt{2I_p}$. In the present work we have considered the ionization energy $I_p = 24.587\,\text{eV}$ (=0.903 56 a.u.) for the $1s$ state of He ($Z_{\text{eff}} = 1.344\,29$).

In order to compute the results presented it was necessary to evaluate $\ell(t)$ [Eq. (15)] considering $\hat{\varepsilon}_X = \hat{z}$ and $\hat{\varepsilon}_L = \hat{x}$. Thus,

$$\begin{aligned}\ell(t) &= -\frac{F_{X0}}{\pi}(2\alpha)^{5/2} \frac{\hat{z}\cdot\mathbf{\Pi}(\mathbf{k},t)}{[\mathbf{\Pi}^2(\mathbf{k},t)+\alpha^2]^3} \\ &= \frac{-F_{X0}(2\alpha)^{5/2}}{[\mathbf{\Pi}^2(\mathbf{k},t)+\alpha^2]^3\pi}\left(\mathbf{k}\cdot\hat{z} + \frac{\mathbf{k}\cdot\mathbf{A}_L(\omega_L t)}{c} + \frac{\mathbf{A}_L^2(\omega_L t)}{2c}\right),\end{aligned} \tag{A3}$$

with $\mathbf{\Pi}^2$ detailed in Eq. (11).

[1] Y. Mairesse and F. Quéré, Frequency-resolved optical gating for complete reconstruction of attosecond bursts, Phys. Rev. A **71**, 011401(R) (2005).
[2] E. Goulielmakis, M. Schultze, M. Hofstetter, V. S. Yakovlev, J. Gagnon, M. Uiberacker, L. A. Aquila, E. M. Gullikson, D. T. Attwood, R. Kienberger, F. Krausz, and U. Kleineberg, Single-cycle nonlinear optics, Science **320**, 1614 (2008).
[3] E. Goulielmakis, M. Uiberacker, R. Kienberger, A. Baltuska, V. Yakovlev, A. Scrinzi, T. Westerwalbesloh, U. Kleineberg, U. Heinzmann, M. Drescher, and F. Krausz, Direct measurement of light waves, Science **305**, 1267 (2004).
[4] J. Gagnon and V. S. Yakovlev, The robustness of attosecond streaking measurements, Opt. Express **17**, 17678 (2009).
[5] M. Drescher and F. Krausz, Attosecond physics: Facing the wave-particle duality, J. Phys. B **38**, S727 (2005).
[6] M. Meyer, J. T. Costello, S. Düsterer, W. B. Li, and P. Radcliffe, Two-colour experiments in the gas phase, J. Phys. B **43**, 194006 (2010).
[7] V. Véniard, R. Taïeb, and A. Maquet, Two-Color Multiphoton Ionization of Atoms Using High-Order Harmonic Radiation, Phys. Rev. Lett. **74**, 4161 (1995).
[8] J. Itatani, F. Quéré, G. L. Yudin, M. Y. Ivanov, F. Krausz, and P. B. Corkum, Attosecond Streak Camera, Phys. Rev. Lett. **88**, 173903 (2002).
[9] A. Maquet and R. Taïeb, Two-colour IR+XUV spectroscopies: The "soft-photon approximation", J. Mod. Opt. **54**, 1847 (2007).
[10] P. Radcliffe, M. Arbeiter, W. B. Li, S. Düsterer, H. Redlin, P. Hayden, P. Hough, V. Richardson, J. T. Costello, T. Fennel, and M. Meyer, Atomic photoionization in combined intense XUV free-electron and infrared laser fields, New J. Phys. **14**, 043008 (2012).
[11] M. Meyer, P. Radcliffe, T. Tschentscher, J. T. Costello, A. L. Cavalieri, I. Grguras, A. R. Maier, R. Kienberger, J. Bozek, C. Bostedt, S. Schorb, R. Coffee, M. Messerschmidt, C. Roedig, E. Sistrunk, L. F. Di Mauro, G. Doumy, K. Ueda, S. Wada, S. Düsterer *et al.*, Angle-Resolved Electron Spectroscopy of Laser-Assisted Auger Decay Induced by a Few-Femtosecond X-Ray Pulse, Phys. Rev. Lett. **108**, 063007 (2012).
[12] T. Mazza, M. Ilchen, A. J. Rafipoor, C. Callegari, P. Finetti, O. Plekan, K. C. Prince, R. Richter, M. B. Danailov, A. Demidovich, G. De Ninno, C. Grazioli, R. Ivanov, N. Mahne, L. Raimondi, C. Svetina, L. Avaldi, P. Bolognesi, M. Coreno, P. O'Keeffe *et al.*, Determining the polarization state of an extreme ultraviolet free-electron laser beam using atomic circular dichroism, Nat. Commun. **5**, 3648 (2014).
[13] S. Düsterer, G. Hartmann, C. Bomme, R. Boll, J. T. Costello, B. Erk, A. D. Fanis, M. Ilchen, P. Johnsson, T. J. Kelly, B. Manschwetus, T. Mazza, M. Meyer, C. Passow, D. Rompotis, L. Varvarezos, A. K. Kazansky, and N. M. Kabachnik, Two-color XUV + NIR femtosecond photoionization of neon in the near-threshold region, New J. Phys. **21**, 063034 (2019).
[14] D. B. Milošević, G. G. Paulus, D. Bauer, and W. Becker, Above-threshold ionization by few-cycle pulses, J. Phys. B **39**, R203 (2006).
[15] D. G. Arbó, K. L. Ishikawa, K. Schiessl, E. Persson, and J. Burgdörfer, Intracycle and intercycle interferences in above-threshold ionization: The time grating, Phys. Rev. A **81**, 021403(R) (2010).
[16] A. K. Kazansky, I. P. Sazhina, and N. M. Kabachnik, Angle-resolved electron spectra in short-pulse two-color XUV+IR photoionization of atoms, Phys. Rev. A **82**, 033420 (2010).
[17] A. A. Gramajo, R. Della Picca, S. D. López, and D. G. Arbó, Intra- and intercycle interference of angle-resolved electron emission in laser-assisted XUV atomic ionization, J. Phys. B **51**, 055603 (2018).
[18] D. G. Arbó, K. L. Ishikawa, K. Schiessl, E. Persson, and J. Burgdörfer, Diffraction at a time grating in above-threshold

ionization: The influence of the Coulomb potential, Phys. Rev. A **82**, 043426 (2010).
[19] D. G. Arbó, K. L. Ishikawa, E. Persson, and J. Burgdörfer, Doubly differential diffraction at a time grating in above-threshold ionization: Intracycle and intercycle interferences, Nucl. Instrum. Methods Phys. Res. Sect. B **279**, 24 (2012).
[20] A. A. Gramajo, R. Della Picca, C. R. Garibotti, and D. G. Arbó, Intra- and intercycle interference of electron emissions in laser-assisted XUV atomic ionization, Phys. Rev. A **94**, 053404 (2016).
[21] A. A. Gramajo, R. Della Picca, and D. G. Arbó, Electron emission perpendicular to the polarization direction in laser-assisted XUV atomic ionization, Phys. Rev. A **96**, 023414 (2017).
[22] R. Della Picca, M. F. Ciappina, M. Lewenstein, and D. G. Arbó, Laser-assisted photoionization: Streaking, sideband, and pulse-train cases, Phys. Rev. A **102**, 043106 (2020).
[23] R. Della Picca, A. A. Gramajo, S. D. López, and D. G. Arbó, XUV+IR photoionization of argon atoms: Selection of sideband orders, J. Phys.: Conf. Ser. **1412**, 042002 (2020).
[24] S. Weber, S. Bechet, S. Borneis, L. Brabec, M. Bučka, E. Chacon-Golcher, M. Ciappina, M. DeMarco, A. Fajstavr, K. Falk, E.-R. Garcia, J. Grosz, Y.-J. Gu, J.-C. Hernandez, M. Holec, P. Janečka, M. Jantač, M. Jirka, H. Kadlecova, D. Khikhlukha *et al.*, P3: An installation for high-energy density plasma physics and ultra-high intensity laser–matter interaction at ELI-Beamlines, Matter Radiat. Extremes **2**, 149 (2017).
[25] U. Elu, T. Steinle, D. Sánchez, L. Maidment, K. Zawilski, P. Schunemann, U. D. Zeitner, C. Simon-Boisson, and J. Biegert, Table-top high-energy 7 μm OPCPA and 260 mJ Ho:YLF pump laser, Opt. Lett. **44**, 3194 (2019).
[26] U. Elu, L. Maidment, L. Vamos, F. Tani, D. Novoa, M. H. Frosz, V. Badikov, D. Badikov, V. Petrov, P. S. J. Russell, and J. Biegert, Seven-octave high-brightness and carrier-envelope-phase-stable light source, Nat. Photon. **15**, 277 (2021).
[27] H. R. Reiss, Limits on Tunneling Theories of Strong-Field Ionization, Phys. Rev. Lett. **101**, 043002 (2008).
[28] H. R. Reiss, Erratum: Limits on Tunneling Theories of Strong-Field Ionization [Phys. Rev. Lett. **101**, 043002 (2008)], Phys. Rev. Lett. **101**, 159901(E) (2008).
[29] H. R. Reiss, The tunnelling model of laser-induced ionization and its failure at low frequencies, J. Phys. B **47**, 204006 (2014).
[30] C. C. Chirilă, N. J. Kylstra, R. M. Potvliege, and C. J. Joachain, Nondipole effects in photon emission by laser-driven ions, Phys. Rev. A **66**, 063411 (2002).
[31] S. Brennecke and M. Lein, High-order above-threshold ionization beyond the electric dipole approximation: Dependence on the atomic and molecular structure, Phys. Rev. A **98**, 063414 (2018).
[32] M. Klaiber, E. Yakaboylu, H. Bauke, K. Z. Hatsagortsyan, and C. H. Keitel, Under-the-Barrier Dynamics in Laser-Induced Relativistic Tunneling, Phys. Rev. Lett. **110**, 153004 (2013).
[33] H. Ni, S. Brennecke, X. Gao, P.-L. He, S. Donsa, I. Březinová, F. He, J. Wu, M. Lein, X.-M. Tong, and J. Burgdörfer, Theory of Subcycle Linear Momentum Transfer in Strong-Field Tunneling Ionization, Phys. Rev. Lett. **125**, 073202 (2020).
[34] S. Fritzsche and B. Böning, Lorentz-force shifts in strong-field ionization with mid-infrared laser fields, Phys. Rev. Res. **4**, 033031 (2022).
[35] J. Maurer and U. Keller, Ionization in intense laser fields beyond the electric dipole approximation: Concepts, methods, achievements and future directions, J. Phys. B **54**, 094001 (2021).
[36] R. Kahvedžić and S. Gräfe, Strong-field approximation with leading-order nondipole corrections, Phys. Rev. A **105**, 063102 (2022).
[37] V. S. Popov, Tunnel and multiphoton ionization of atoms and ions in a strong laser field (Keldysh theory), Phys.-Usp. **47**, 855 (2004).
[38] W.-C. Jiang, M.-X. Wang, L.-Y. Peng, and J. Burgdörfer, Signatures of stabilization in the angle-resolved photoemission by an ultrashort intense XUV laser pulse, Phys. Rev. A **105**, 023104 (2022).
[39] K. Lin, S. Brennecke, H. Ni, X. Chen, A. Hartung, D. Trabert, K. Fehre, J. Rist, X.-M. Tong, J. Burgdörfer, L. P. H. Schmidt, M. S. Schöffler, T. Jahnke, M. Kunitski, F. He, M. Lein, S. Eckart, and R. Dörner, Magnetic-Field Effect in High-Order Above-Threshold Ionization, Phys. Rev. Lett. **128**, 023201 (2022).
[40] X. Mao, H. Ni, X. Gong, J. Burgdörfer, and J. Wu, Subcycle-resolved strong-field tunneling ionization: Identification of magnetic dipole and electric quadrupole effects, Phys. Rev. A **106**, 063105 (2022).
[41] S. Chelkowski, A. D. Bandrauk, and P. B. Corkum, Photon Momentum Sharing between an Electron and an Ion in Photoionization: From One-Photon (Photoelectric Effect) to Multiphoton Absorption, Phys. Rev. Lett. **113**, 263005 (2014).
[42] B. Willenberg, J. Maurer, B. W. Mayer, and U. Keller, Subcycle time resolution of multi-photon momentum transfer in strong-field ionization, Nat. Commun. **10**, 5548 (2019).
[43] A. Hartung, S. Eckart, S. Brennecke, J. Rist, D. Trabert, K. Fehre, M. Richter, H. Sann, S. Zeller, K. Henrichs, G. Kastirke, J. Hoehl, A. Kalinin, M. S. Schöffler, T. Jahnke, L. P. H. Schmidt, M. Lein, M. Kunitski, and R. Dörner, Magnetic fields alter strong-field ionization, Nat. Phys. **15**, 1222 (2019).
[44] B. Böning and S. Fritzsche, Above-threshold ionization driven by Gaussian laser beams: Beyond the electric dipole approximation, J. Phys. B **54**, 144002 (2021).
[45] C. Joachain, N. Kylstra, and R. Potvliege, *Atoms in Intense Laser Fields* (Cambridge University Press, Cambridge, 2012).
[46] M. Lewenstein, P. Balcou, M. Y. Ivanov, A. L'Huillier, and P. B. Corkum, Theory of high-harmonic generation by low-frequency laser fields, Phys. Rev. A **49**, 2117 (1994).
[47] K. Amini, J. Biegert, F. Calegari, A. Chacón, M. F. Ciappina, A. Dauphin, D. K. Efimov, C. F. de Morisson Faria, K. Giergiel, P. Gniewek, A. S. Landsman, M. Lesiuk, M. Mandrysz, A. S. Maxwell, R. Moszyński, L. Ortmann, J. A. Pérez-Hernández, A. Picón, E. Pisanty, J. Prauzner-Bechcicki *et al.*, Symphony on strong field approximation, Rep. Prog. Phys. **82**, 116001 (2019).
[48] M. Lewenstein, K. C. Kulander, K. J. Schafer, and P. H. Bucksbaum, Rings in above-threshold ionization: A quasiclassical analysis, Phys. Rev. A **51**, 1495 (1995).
[49] S. Nagele, R. Pazourek, J. Feist, K. Doblhoff-Dier, C. Lemell, K. Tokési, and J. Burgdörfer, Time-resolved photoemission by attosecond streaking: Extraction of time information, J. Phys. B **44**, 081001 (2011).
[50] R. Della Picca, J. Fiol, and P. D. Fainstein, Factorization of laser–pulse ionization probabilities in the multiphotonic regime, J. Phys. B **46**, 175603 (2013).

[51] D. Wolkow, Uber eine klasse von lösungen der Diracschen gleichung, Z. Phys. **94**, 250 (1935).

[52] S. V. B. Jensen, M. M. Lund, and L. B. Madsen, Nondipole strong-field-approximation Hamiltonian, Phys. Rev. A **101**, 043408 (2020).

[53] J. Hummert, M. Kubin, S. D. López, J. I. Fuks, F. Morales, M. J. J. Vrakking, O. Kornilov, and D. G. Arbó, Retrieving intracycle interference in angle-resolved laser-assisted photoemission from argon, J. Phys. B **53**, 154003 (2020).